Proceedings World Geothermal Congress 2015
Melbourne, Australia, 19-25 April 2015

Flow Lognormality and Spatial Correlation in Crustal Reservoirs: II – Where-to-Drill Guidance via Acoustic/Seismic Imaging

Peter Malin, Peter Leary, Eylon Shalev, John Rugis, Brice Valles, Carolin Boese, Jennifer Andrews & Peter Geiser

Institute of Earth Science & Engineering, University of Auckland, New Zealand

p.leary@auckland.ac.nz

Keywords: EGS, reservoir flow, permeability stimulation, fracture stimulation, spatial correlation, lognormality

ABSTRACT

Roughly 7-10 geothermal wells are drilled in order to provide 1 well producing enough steam to drive a turbine. This well-drilling sunk cost is, however, far from unique to geothermal reservoirs. Rather it is endemic to crustal reservoirs of all fluid types: convention and non-conventional hydrocarbon, groundwater, fossil flow mineralisation, as well as geothermal. E.g., representative of the vast statistical data for onshore oil field well productivity, in the year 2009 the state of Texas had 60 wells producing an average of 645 barrels/day, 2984 wells producing an average of 88 barrels/day, and 80770 oil field wells producing an average of 1 barrel/day. As there is no intrinsic reason to consider geothermal fields significantly different from oil fields (except that the pay fluids are different), the multi-state multi-year US oil field well producer statistics are strong indicators of how rare it is to drill crustal reservoir 'producers': for purely blind drilling, for every geothermal producer, the intrinsic odds are for 50 non-producers (with an additional 1300 wells that would never be considered for drilling). At $100/barrel value of oil, oil field well sunk costs are manageable. At $1/barrel value of hot water, geothermal drilling sunk costs requires a fundamentally different well drilling strategy. Historically geothermal wells are drilled with reference to surface manifestations and geological interpretations of subsurface structure. Given what lognormal-distribution well productivity data tell us about the strong heterogeneity of reservoir flow systems, we can assert that we need greatly improved subsurface flow structure data to guide the drill bit to achieve more cost-effective hydrothermal heat extraction. We can take the necessary step by looking below the reservoir surface via innovative use of standard multi-channel seismic sensor array technology as deployed over shale body reservoirs subjected to repeated massive hydrofracture treatments along horizontal wellbores. Unlike oil field flow systems, which are non-flowing until disturbed by reservoir operations, geothermal reservoir flow systems are naturally acoustically noisy, with the noise levels scaling in rough proportion to the volume of naturally occurring fluid flow. Surface sensor array data have demonstrated that acoustic noise generated by shale body fracking practice contain sufficient signal levels that specialised use of otherwise standard seismic processing technology can reliably locate a large range of reservoir subsurface flow structures, most importantly the large-scale reservoir flow patterns associated with large-scale but spatially elusive fracture channels endemic to crustal rock. While the dismal oil field well productivity statistics amply reflects the deficiency of drilling without valid information about subsurface flow targets, it is now possible to identify the fundamental physical reason behind poor well productivities, take technical steps to acquire necessary reservoir flow structure information, and actively upgrade drill site locations to guide the drill bit to the main flow structures in the reservoir fracture system.

1. INTRODUCTION

Crustal flow structures tend to be lognormally distributed. That is, *in situ* fluid flow tends to be dominated by a relatively small number of large-scale/high-flux systems amidst a relatively large number of small-scale/low-flux systems. An operational consequence of lognormally distributed in situ flow systems is that reservoir well drilling is often highly inefficient. While the lognormal statistical features of reservoir flow have been apparent for decades, recognition of underlying physical causes, and hence possible physics-based remedies, has been considerably slower in coming. We outline here a physical approach to *in situ* flow system lognormality that provides a physics-based observational scheme for improved well-siting at geothermal reservoirs

In common with crustal reservoirs at large, the size distribution of geothermal fields is lognormally distributed in size (Fig 1).

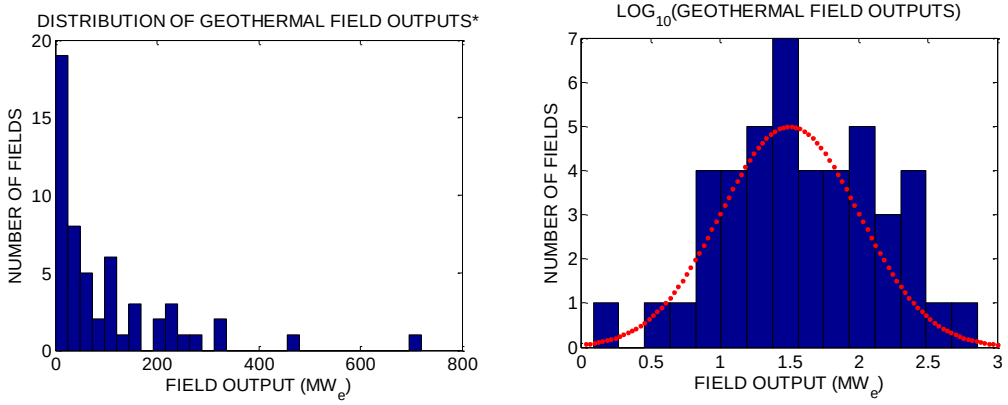

Fig 1. The strongly skewed distribution of worldwide geothermal field electrical power output (left; 2GW$_e$ Geysers outlier omitted) is seen to be lognormal (right), with mean 30MW$_e$ and median 50MW$_e$. Data from IFC(2013).

Oil/gas-field and mineral-deposit sizes have long been known to be lognormally distributed (Kaufman 1963; Ahrens 1963; Gerst 2008). Lognormal distributions are characteristic of permeability and well-flow populations within both hydrocarbon reservoirs (Leary et al. 2012, 2014; USEIA 2011) and geothermal fields (Grant 2009; Leary et al. 2013). Further to the well flow statistics within individual geothermal fields, Fig 2 shows that the population of 'successful' wells is lognormally distributed.

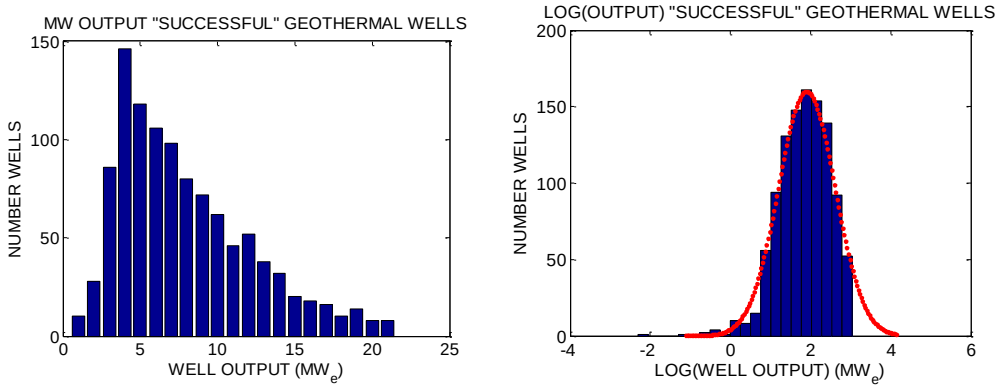

Fig 2. (Left) Skew distribution of MW_e output from 'successful' wells in geothermal fields worldwide. (Right) Lognormality of 'successful' well skew distribution. Data from IFC (2013).

When compared with non-selective lognormality data of Fig 1, however, the Fig 2 distribution can be considered as grossly misleading: for every 'successful' geothermal well there are many 'unsuccessful' wells rarely cited in geothermal literature. Corrections for the 'unsuccessful' well population count omitted from Fig 2 but implied by Fig 1 and related statistical distributions can be estimated by lognormally extrapolating the "successful" well distribution as indicated in Fig 3. The black curve of Fig 3 is consistent with an estimated 25% overall geothermal drilling 'success' rate compared with an estimated 50% success rate for oil field wildcat drilling (*Petroleum Economist* 2009). The large unsuccessful well count missing from Fig 2 is a significant sunk cost to geothermal energy.

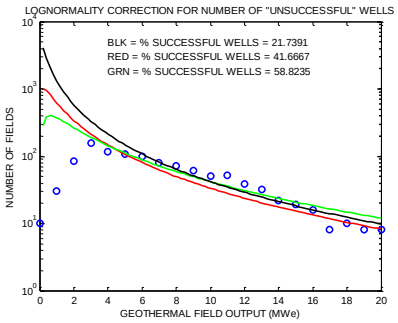

Fig 3. Corrections to Fig 2 'successful' well distribution curve (blue circles) to account for the large missing count of 'unsuccessful' wells drilled in order to achieve the Fig 2 population of 'successful' wells. The black correction curve, consistent with the Petroleum Economist 2009 estimate of 25% geothermal well 'success', renders the Fig 2 distribution consistent with Fig 1 reservoir flow structure size distributions.

A parallel cost of ineffective well siting is associated geothermal field output declines, as seen in Fig 4 for the Geysers field in California. During 1985-2005, Geysers output declined 50% from peak production due to falling *in situ* water pressure. The falling pressure trend has in recent years been arrested but not reversed by a major re-injection programme. In some measure failure to reverse the decline can be attributed to not knowing where to drill effective injector wells.

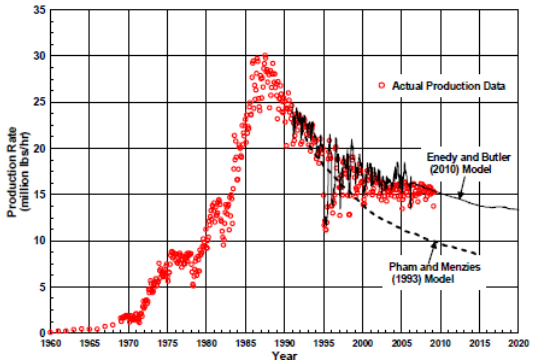

Fig 4. Geysers field output 1960-2010. Pre-1985 outputs reflect increased well numbers. Post-1985 output decline reflects draw-down of a finite fluid reservoir. Addressing fluid draw-down is hampered by inability to properly locate injection wells to restore withdrawn fluid. Data from Sanyal & Enedy (2011).

2. SPATIAL HETEROGENEITY OF RESERVOIR WELL PRODUCTION/PRODUCTIVITY

We can approach improved geothermal well siting by considering well production heterogeneity documented for the shale reservoirs. Inability to more effectively site geothermal wells likely reflects the inherent fracture-nature *in situ* flow in the crust at large rather than any specific property of geothermal systems. Crustal fracture systems are generated in the brittle crust by on-going large-scale tectonic deformation arising more or less directly from mantle convection (Leary et al 2014). While geothermal systems are directly associated with heat brought to the surface by mantle mechanics – continental and oceanic rift systems as in Africa, western US, Mexico and Iceland, and oceanic plate subduction as in Japan, Philippines, Indonesia, and New Zealand – geothermal heat flux is fluid-borne via brittle crust fracture systems common to crustal reservoirs fluid flow systems worldwide. Fracture-system commonality of *in situ* fluid flow system complexity results in the large number of 'unsuccessful' wells at reservoirs everywhere.

Figs 5 displays production data for 50 lateral wells in a 5km-by-8km shale reservoir section. Oil and gas production magnitude at each well site is denoted by a disk of proportionate area and tint (warmer=larger; cooler=smaller). At left is the observed spatial array of lognormally distributed well-production magnitudes in which a few wells dominate production for the section. For comparison, the center plot shows the nature of well-production for an assumed uncorrelated/Gaussian randomness of production magnitude. The right-hand plot shows the observed well productivity magnitude distribution to be lognormal.

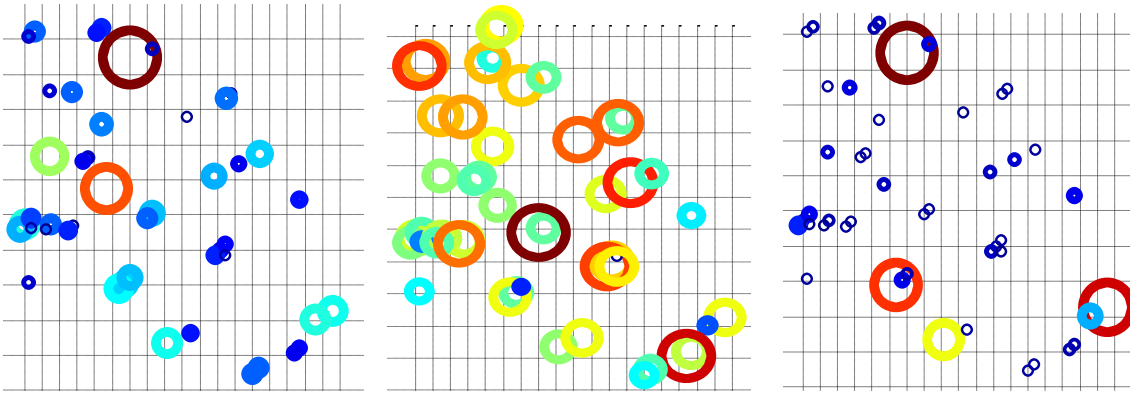

Fig 5. Spatial distribution of well production (left/center) and well productivity (right) over a 5km by 8km horizontal shale reservoir section. The observed spatial distribution of lognormal population of shale reservoir well production (left) is contrasted visually with the same spatial distribution realised for a hypothetical normally distributed well production population (center). As with well production, well productivity (right) is also lognormally distributed.

Gaussian randomness implies a considerably larger population of large-area/warm-tint entries than do the lognormally-distributed field data. In the Fig 5 left/center plots each population has a maximal-area/deep-red entry but where the Gaussian random population has 2 small/deep-blue (low production) entries, the field data have ~20 such entries. Fig 5 field data make clear that statistical characterization of reservoir well data as Gaussian randomness – characterised by population and sample means and standard deviations – is inherently inaccurate when applied to *in situ* well production. Accurate assessment of risk and uncertainty of future well siting and production based on existing well performance data accordingly demands more observational rigor than provided by sample means and standard deviations appropriate to uncorrelated/Gaussian randomness.

The Fig 5 left/center well production magnitude distributions indicate that an *in situ* physical process of spatial correlation exists within crustal volume flow property distributions. In contrast with the formally uncorrelated Gaussian population of well-production sizes in the center plot, the population of observed 20 or so low-production well sites in the left-hand plot bespeaks a tendency for a low production well to be near another low production well. Such magnitude correlations can be dismissed as statistically trivial – there being many more low-producing wells than high producing wells – but history has shown that a purely statistical assessment has not eliminated well-siting inefficiency. We are prompted to ask if there is non-trivial physical process lying behind the spatial correlations that may be said to necessarily arise in lognormal distributions.

Fig 6 gives observational evidence for a physical-property correlation within the Fig 5 shale reservoir well population. The upper left/right and lower-left plots of Fig 6 show that the shale reservoir well population has a tendency for well productivity – plausibly related to *in situ* permeability in the crustal volume drained by the well – to scale with well production – plausibly related to *in situ* porosity in the crustal volume drained by the well. For each well group, low-production wells are associated with low-productivity wells, while high-production wells are associated with high-productivity wells. The productivity/production ≡ permeability/porosity scaling trend is independent over a decade of production size, indicating that that the data do not represent accidents of purely geological origin; i.e., the data do not invite us to suppose large reservoir units (= high production) have an affinity for high permeability (= high productivity) while small reservoir units (= low production) have an affinity for low permeability (= low productivity). The lower-right plot of Fig 6 establishes that the same trend exists on the much larger scale of US statewide onshore oil/gas production: an eclectic large-scale population of crustal reservoirs shows a marked tendency for high production wells to be associated with high production-rate well flow and for low production wells to be associated with low production-rate well flow.

§3 discusses the empirical physics by which weaker high porosity reservoir volumes are more subject to finite-strain damage than are low porosity volumes, thus creating comparatively more fracture-related fluid pathways that promote permeability/productivity in association with porosity/production. These physical empirics underpin the reservoir flow-system mapping presented in §4.

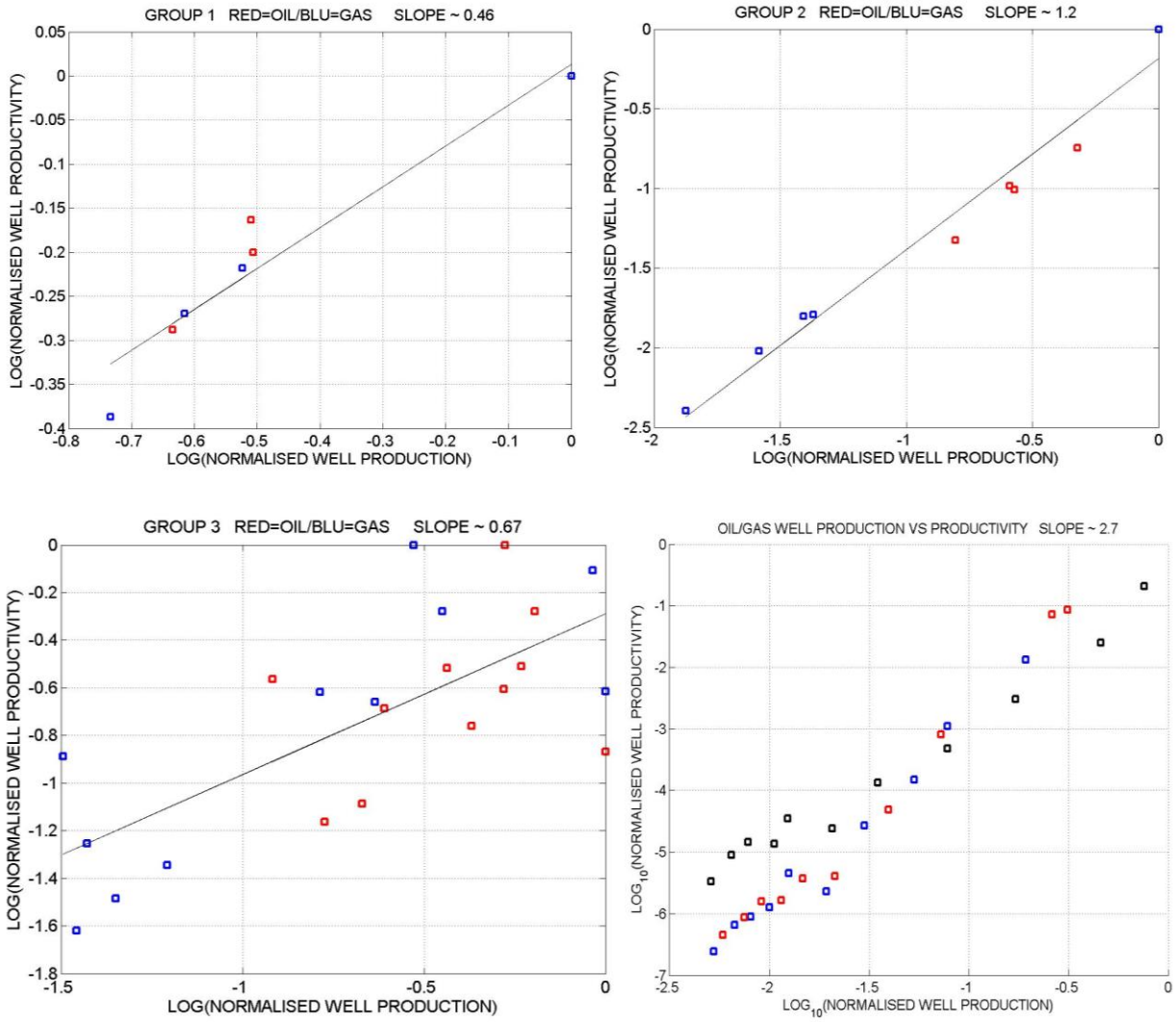

Fig 6. (Upper-left to lower-left) Decadal scaling trends for Fig 5 population of shade reservoir well production (nominally related to *in situ* porosity) and well productivity (nominally related to *in situ* permeability). The lower-right plot extends the data base of this trend to US statewide oil/gas fields, here represented by Yr2009 samples from CA (red), OK(black) and TX(blue) (data from USEIA 2011). As discussed in §2, the observed scaling trends can be interpreted to mean that *in situ* reservoir sectors that are more/less porous are also subject to more/less finite-deformation damage leading to more/less ability of fluids to percolate through grain-scale fracture networks in the brittle-fractured crust.

3. THE GEOCRITICAL RESERVOIR

Three empirical properties are observed to apply to crustal reservoirs worldwide:

1) Long-range spatial correlations seen in power-law spectral scaling of well-log spatial fluctuations;
2) Intimate spatial relation between grain-scale fracture density (related to porosity) and grain-scale fracture-connectivity (related to permeability) seen in a close spatial fluctuation relation between well-core porosity and the logarithm of well-core permeability;
3) Fracture-connectivity spatial percolation networks at all scales seen in lognormal distributions of well-productivities.

Together the three properties define a 'geocritical reservoir', where 'critical' refers to the 'critical' density of grain-scale fractures in the crust leading to tendency for crustal volumes to have a through-going percolation backbone at all scales from grains to reservoirs (Leary 1997, 2002). The trio of physical tenets defining the geocritical reservoir connect the Figs 1-4 lognormality phenomenology of well production/productivity – and its associated drilling inefficiency – to the technology of recording and processing background and/or stimulated seismic/acoustic energy release within reservoir volumes.

(1) Long-range spatially correlated flow structures – 1/k spectral scaling of gamma-active solute abundances

The advent in the mid-80s of digital well logs enabled recognition of a previously unknown systematic feature of *in situ* spatial fluctuations in rock properties. In parallel with recognition of the fractal nature of many geological processes (conspicuously those

related to fractures) it was seen that the Fourier power-spectra of well logs systematically scaled inversely with spatial frequency over five decades of scale length,

$$S(k) \propto 1/k^{\beta},\ \beta \sim 1,\ \sim 1/\text{cm} < k < \sim 1/\text{km}, \qquad (1)$$

where $S(k)$ is the squared-amplitude or power at spatial frequency k of the spatial fluctuations measured by well-log physical property sequence. Spectral behaviour (3) spanning grain-scales to reservoir-scales is observed to apply equally to essentially all well-logged properties, all geological settings, and both vertical and horizontal wells (Hewett 1986; Leary 1991, 2002a; Leary et al 2013; Dolan, Bean & Riollet 1998; Marsan & Bean 1999; Shiomi, Sato & Ohtake 1997). The natural interpretation of (3) is in terms of fractures from the grain-scale to reservoir-scale in parallel with extensive documentation of the fractal nature of fractures (e.g., King 1983; Turcotte 1986; Hirata 1989; Leary 1991), as well as the phenomenology of low-stress induced seismicity (e.g., Simpson 1976; Simpson & Negmatullaev 1980; Simpson, Leith & Scholz 1988; Gupta 2002), recognition that *in situ* seismic scattering points to crustal fractures at all scale lengths in the brittle-fracture upper crust (Leary & Abercrombie 1994a-b; Leary 2002a-b), and the inferred existence of grain-scale stress sensitivity evidenced by stress-aligned seismic anisotropy everywhere (Crampin 1994) and intrinsic seismic attenuation via grain-grain contact stresses (Leary 1995).

As an example of well-log spectral scaling (1), Fig 7 shows spectra for spatial fluctuations in gamma ray activity from solute minerals dispersed via fluid percolation flow in crustal fracture-connectivity networks recorded over ~km at 2m sample intervals. The upper two Fig 7 spectra are from lateral wells in a shale reservoir, and the below trio are from vertical wells in the Los Azufres geothermal field in central Mexico (Leary et al 2013).

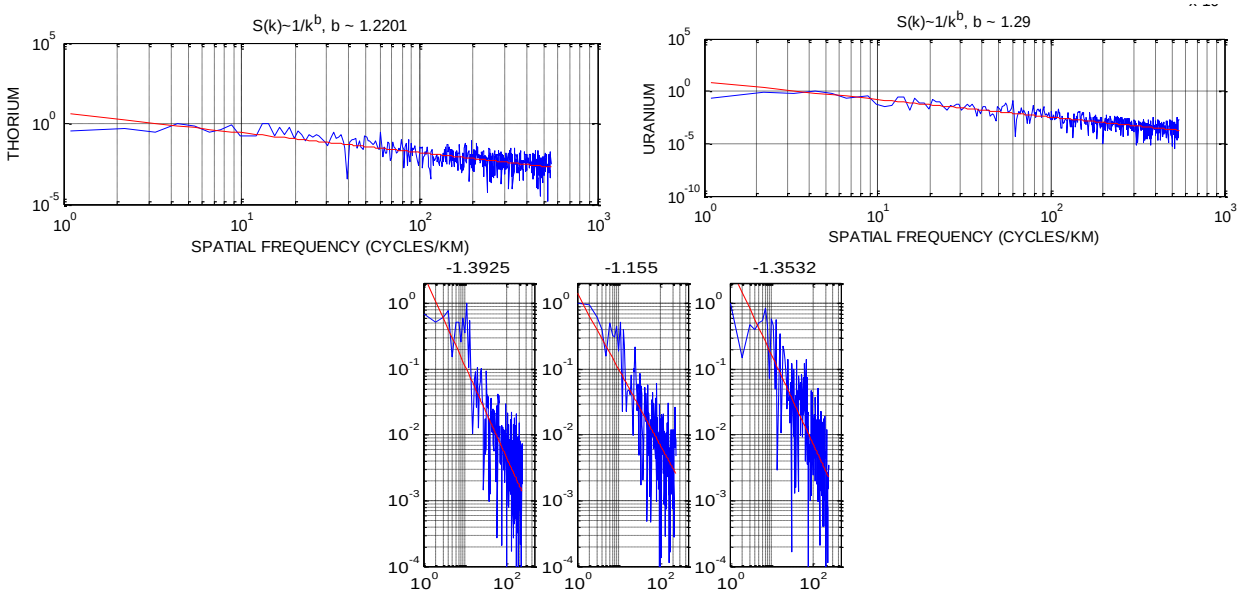

Fig 7. The spatial frequency scaling of flow-distributed solute abundances in a shale reservoir (upper) and a geothermal field (lower). The well-log physical variable in all spectra is gamma activity due to thorium-, uranium-, and potassium bearing solute minerals. The sample of well-log spectra of solute distributions scale inversely with spatial frequency k over ~2.7 decades, $S(k) \propto 1/k^{\beta}$, $\beta \sim 1.28 \pm 0.11$.

(2) *Grain-scale fracture density & fracture-connectivity; well-core fluctuations of porosity & permeability*

Fig 8 illustrates the intimate spatial relation between porosity and log(permeability) widely documented in clastic reservoir well-core sequences (left-hand plots), and the less well documented but statistically significant relation between porosity and log(permeability) in geothermal well-core sequences (right-hand plots). Blue/red overlain traces indicate spatial fluctuations in well-core porosity and logarithm of well-core permeability, respectively. The porosity/log(permeability) trace overlays of Fig 8 express the empirical spatial fluctuation relation

$$\delta\varphi \propto \delta log(\kappa), \qquad (2)$$

in which $\delta\varphi$ and $\delta\log(\kappa)$ denote spatial fluctuations in well-core porosity and in the logarithm of well-core permeability along the well-core depth sequence. The proportionality relation can be refined to near equality, $\delta\varphi \approx \delta log(\kappa)$, by normalising each data sequence to zero-mean/unit-variance form given as Fig 8 blue/red trace-overlays. The histograms of the Fig 8 left-hand data illustrate the lognormality of well-core permeability distributions.

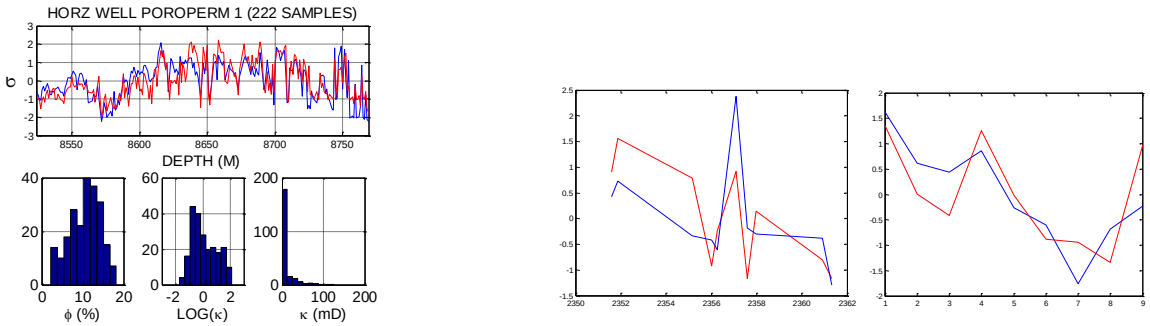

Fig 8. Spatial fluctuation relation between well-core porosity (blue) and logarithm of well-core permeability (red) for a North Sea classic reservoir well-core sequence (left) and two geothermal well-core sequences from Ohaaki NZ and Bulalo PH respectively (2 x right). The North Sea data indicates that well-core porosities are normally distributed while the permeabilities are lognormally distributed.

Well-core poroperm fluctuation relation (2) can be understood in terms of a fluctuating number of grain-scale fractures, $\varphi \propto n$, in each well-core and a corresponding fluctuating grain-scale fracture connectivity by which permeability increases with grain-scale fracture number n in proportion to the factorial of the grain-scale number, $\kappa \propto n!$. Substitution of n and $n!$ yields the fluctuation relation $\delta n \propto \delta log(n!)$, which is essentially Stirling's identity expressing the logarithm of factorial $n!$ in terms of n, $log(n!) \sim nlog(n) - n$. Empirical well-core poroperm fluctuation relation (2) is thus consistent with a picture of fluid flow by grain-scale percolation in which flow is proportional to the number of ways in which the number of defects n can be linked in space, $n!$. The logarithm in (2) gives rise to the lognormal-skew nature of *in situ* permeability distributions, to which we can give a physical interpretation as fracture interactions via which fracture connectivity controls the ease with which *in situ* fluids flow along fracture-connectivity pathways at all scales. Power-law scaling empirical relation (1) indicates that the larger the physical scale of the fracture-connectivity pathway, the greater the flux carried by the pathway. Lognormal-like skew of *in situ* flow systems thus naturally emerges from widely-attested physical properties of crustal rock.

(3) Fracture-connectivity percolation networks at all scales – lognormal distributions of well-productivities

Spatially integrating empirical relation (2) along a well-core sequence gives macroscopic permeability $\kappa(x,y,z)$ as a spatial function of macroscopic porosity $\varphi(x,y,z)$,

$$\kappa(x,y,z) \propto \exp(\alpha\varphi(x,y,z)), \qquad (3)$$

where α is an integration constant denoting the empirical ratio between spatial variation in $\log(\kappa)$ and spatial variation in φ. The significant of parameter α is seen in Fig 9, where a fixed (normal) distribution of porosity $\varphi(x,y,z)$ yields a series of distributions of permeability $\kappa(x,y,z)$ depending on the value of α. For α small, (3) returns normal distributions, seen the upper row of Fig 9. As α grows in magnitude, (3) returns evermore lognormal distributions, ending in the strongly lognormal distribution seen in the lower right corner of Fig 9.

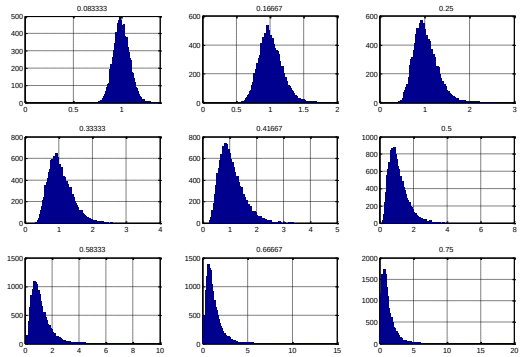

Fig 9. Progression from normal distributions (upper left) to lognormal distributions (lower right) of *in situ* permeability $\kappa(x,y,z)$ given by (3) as a function of empirical integration parameter α for a fixed distribution of *in situ* porosity $\varphi(x,y,z)$. Values of $\alpha < 10$ give normal-to-near-normal permeability distributions; observed values of α in range $30 < \alpha < 60$ correspond to increasingly lognormal permeability distributions observed in reservoirs everywhere.

Empirically observed lognormal distributions occurring in the lower right corner of Fig 9 have values of α in the range 30 to 60 for the standard 0.1-0.35 range of *in situ* porosity. Fig 9 thus shows how well-core-scale microscopic fluctuation porosity-permeability relation (2) lies at the origin of the macroscopic lognormal well-flow distributions of Figs 1-5. Note in Fig 9 that for a fixed range of porosities, *in situ* permeability increases by an order of magnitude as α increases in value from the upper left to lower right of Fig 9. We see that the limited and largely unchanging range of *in situ* porosity accounts for the practically unlimited range and potentially high degree of changeability of *in situ* permeability via the one-parameter function (3) interpreted as the degree of grain-scale fracture-connectivity within a crustal volume. Values of fracture-connectivity parameter α typically in the range $30 < \alpha < 60$ (Leary, Pogacnik & Malin 2012) accord with clastic reservoir well-core and well-flow data everywhere (Law 1944; de Wijs 1951,

1953; Ahrens 1963; Warren & Skiba 1964; Bennion & Griffiths 1966; Koch & Link 1971; Zikovsky & Chah 1990; Mabee 1999; Leary & Al-Kindy 2002; Ricciardia, Pinder & Belitz 2005; Gerst 2008; Grant 2009; Maharjan 2011; USEIA 2011).

For the 'critical state' crust outlined in Figs 1-9, there is long-standing evidence that *in situ* fracture-connectivity flow structures are locally sensitive to small changes in fluid pressure (Simpson 1976; Simpson & Negmatullaev 1980; Simpson, Leith & Scholz 1988; Gupta 2002; Pollard & Segall 1987; Segall 1989; Ziv & Rubin 2000). More recently, small changes in the fluid pressure of geocritical state reservoirs are discernable via acoustic emissions that occur preferentially along large-scale percolation fracture-connectivity pathways (Geiser et al 2006a-b, 2012). Systematic detection of these incidental acoustic emissions leads to reliable, repeatable, and physically interpretable *in situ* flow structure maps within a reservoir that supplant statistical inferences as guides to where to drill in order to intersect the main reservoir flow structures.

4. SURFACE ARRAY SEISMIC MONITORING OF THE GEOCRITICAL RESERVOIR

We now describe the surface seismic-array observational means established by Geiser et al (2006a-b, 2012) to address well-drilling inefficiency associated with high degrees of reservoir flow structure uncertainty arising from 'critical state' spatially-erratic fracture-connectivity in crustal rock.

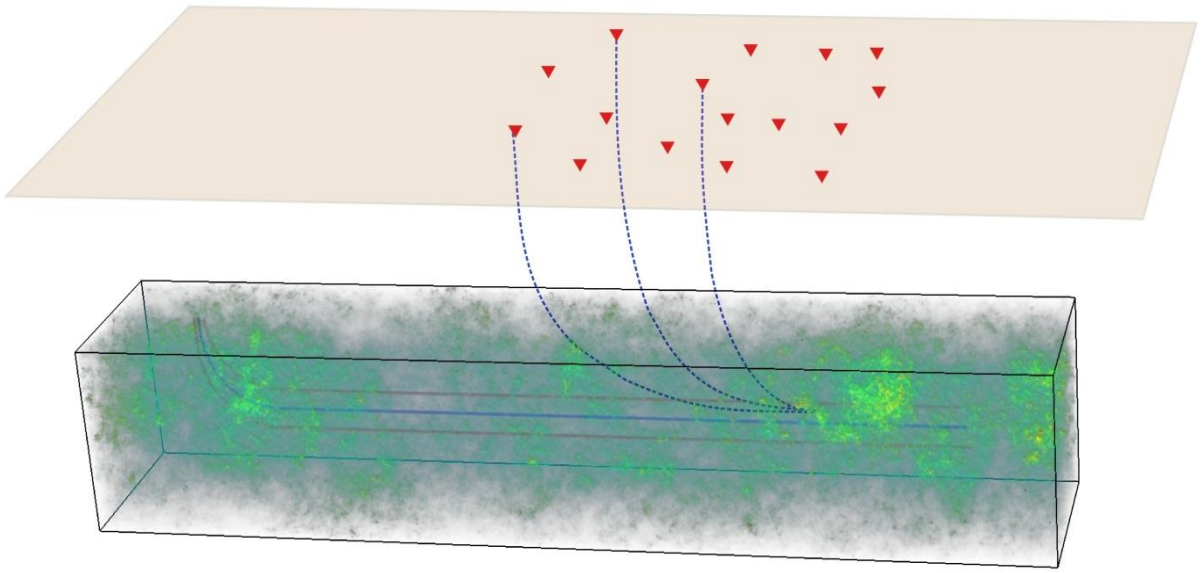

Fig 10 – A spatial distribution of crustal porosity and associated fracture density is numerically realised for a rectilinear volume of 1km lateral dimension and 96m x 96m cross-section. The spatial distribution of porosity is governed by empirical spectral scaling relation (1); the associated permeability and flow structure of the volume are given by empirical poroperm relations (2)-(3), with the value of fracture-connectivity parameter α in (3) large enough to ensure lognormality of the crustal flow structure. The crustal poroperm volume lies at reservoir depth below a surface array of seismic sensors (red triangles). Small seismic events associated with fluid pressure changes in the crustal volume emit seismic energy that can be recorded by surface sensors. Acquisition of sufficient seismic data by a sufficient number of sensors enables very small *in situ* slip events to be back-located in the crustal volume. The fact that higher porosity regions are more likely to host slip events enables the back-located event population to 'map' the high porosity regions of a reservoir volume, thus providing drilling targets.

Fig 10 shows a rectilinear crustal volume below a surface array of seismic sensors denoted by red triangles. The crustal volume depicts numerical realisation of long-range spatial-correlation expressed by empirical eqs (1)-(3) and leading to reservoir uncertainty (e.g., Figs 1-5). As prescribed by spectral scaling relation (1), portions of a crustal volume have higher density porosity and grain-scale fracture density, given here as light green clustering, along regions of lower density porosity/fracture-density represented by dark/blue-green clustering. In line with empirical relations (2)-(3) and Fig 6 well production/productivity trends, light green portions of the crustal volume are associated with greater well production/productivity, and dark/blue-green regions with lesser well production/productivity. While the location of the light/dark green clustering is random and unpredictable from any form of small-scale sampling, seismic data arising from the critical-stress nature of the crustal volume can locate the more porous/fluid-rich clusters as drilling targets. Fluid pressure disequilibrium creates more flow in the porous (i.e., light green) regions relative to the less porous (i.e., dark green) regions. In response to fluid disequilibrium, the critically-stressed elements in the active flow regions of the crustal volume can shift slightly, emitting seismic energy that propagates to the surface (blue dotted lines Fig 10). With a sufficient number of surface sensors and a long enough recording time, the very low level seismic events associated with pressure-disequilibrium flow can be extracted from seismic background and back-traced to their spatial origin. Fig 11 synopsizes the multi-channel seismic data analysis that leads to the Fig 12-15 shale reservoir monitoring images.

The seismic signals issued by low-level reservoir instability slips triggered by *in situ* pressure variations are too small to be directly observed on the surface seismic array sensors. However, small seismic events registered on many seismic recording channels can be detected by systematically combing through the multi-channel recorded data as outlined in Fig 11 for a 9 x 9 surface seismic array such as indicated by the red triangles of Fig 10. For any given interval of seismic data recording time – say 100 milliseconds – each sensor records background seismic activity which may, or may not, include a small seismic event arrival from the reservoir

volume. The left-hand panel of Fig 11 simulates one such arrival across a 9 x 9 sensor array in the absence of seismic noise. Events with arrivals at multiple sensors as illustrated in Fig 11 are detected and back-located in space as follows:

- Assume the event arose in a particular node or voxel within the reservoir volume;
- Using a pre-computed travel-time table, look up the travel time from the particular node to each sensor, and shift each seismogram according to the computed travel time such the expected arrival occurs at the earliest window time;
- Sum/stack all such time-shifted seismograms to evaluate one of three options:
  a) If the event arose in the particular node/voxel, each time-shifted initial seismic motion will be aligned for all sensors, and the summed/stacked seismogram will have a large initial arrival as in Fig 11 right-hand upper trace;
  b) If the event arose near the particular node/voxel, each time-shifted initial seismic motion will be partially aligned for some but not all of the sensors;
  c) If the event arose away from the particular node/voxel, the time-shifted initial seismic motions will not be aligned and the summed/stacked seismogram will have no statistically significant peak as in Fig 11 right-hand lower trace;
- If the summed/stacked seismogram has a 'signal' of sufficient level, add a weighted 'semblance' value to the particular node/voxel as with the coloured dots in Fig 12; otherwise add nothing to the node/voxel as in the blank spaces in Fig 12;
- Repeat the time-shift winnowing sequence for the next node/voxel until all nodes/voxels are processed, yielding images such as shown in Figs 12-13.

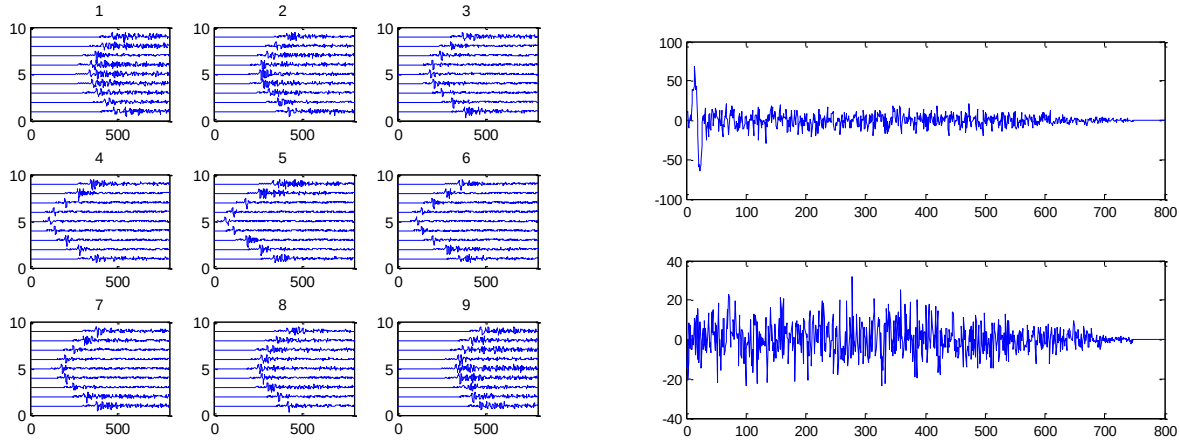

Fig 11. (Left) Keyed to Fig 10, a snap-shot of a long temporal sequence of seismic data recorded by a 9 x 9 array of surface seismic sensors arising from a single source at depth in the reservoir volume. The array data display shows the event without background noise; in a realistic simulation of seismic data processing, each signal is presumed buried in background noise ten or more times the magnitude of the largest event signal. (Right) Seismic data processing involves shifting each of the left-hand-panel traces back and forth along its time axis according to the following logic: (a) If trace X contains a signal from a hypothetical event at source location Y, then if that trace is shifted by T_{XY} units in time, T_{XY} = the travel-time between source sensor X and source location Y, the signal should be shifted to the beginning of record; (b) Summing all traces X time shifted by amounts T_{XY} for an actual source at location Y adds traces constructively to produce an identifiable net signal (initial spike in upper trace); (c) Summing all traces X time shifted by amounts T_{XY} for an non-existent source at location Y adds traces destructively to produce a noise sequence (absence of initial spike in lower trace). Note the higher seismogram count for the upper versus lower composite traces shown in the right-hand panel. Seismic data processing repeats the trace-by-trace time-shift procedure for every small time window in a recording sequence for every source location with a 3D mesh representation of the reservoir. A typical data processing scan for a reservoir monitoring data set recorded over a 3 hour period may involve 100000 time windows, 50000 source-point nodes, and 100-300 sensors for order ~1T seismogram time-shift operations.

Fig 12 shows a representative poroperm seismic semblance image recorded by a surface seismic array deployed over a producing shale reservoir invested with a 1.5km horizontal wellbore (black line) at ~2.5km depth. Each colored grid point in Fig 12 represents the location of a source point within the shale reservoir that has registered a sufficient degree of event semblance by the seismic data processing sequences outlined in Fig 11. Warmer to cooler colors denote greater to lesser event semblance signal size as given by the initial semblance signal spike in the upper-right trace of Fig 11. Reservoir nodes without significant semblance signal remain blank.

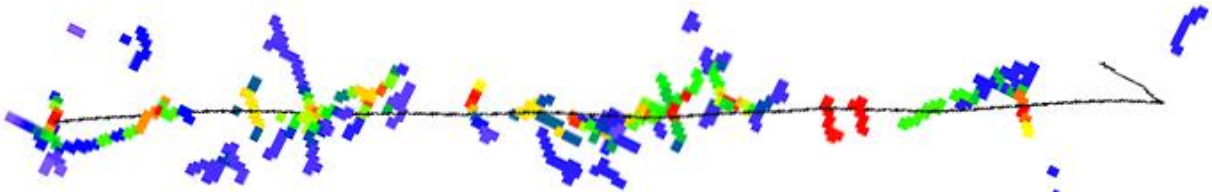

Fig 12. Shale reservoir wellbore seismic semblance sequence along wellbore. Colored dots denote spatial distribution of semblance magnitude; warm colors are higher semblance, cool colors are lower semblance; white background denotes absence of significant semblance signal.

The connection between semblance distributions illustrated in Figs 12-13 and *in situ* fluid-pressure processes and associated permeability pathways has been documented by Geiser et al (2006a-b, 2012). The connection should not be surprising. Pressures of 1bar ≡ 10m or smaller due to ponding water over some km of crustal surface tend to trigger earthquakes in ordinary crust (Simpson 1976; Simpson & Negmatullaev 1980; Simpson, Leith & Scholz 1988; Gupta 2002). It is also known that both extracting and injecting relatively small amounts of *in situ* fluid from crustal volumes induce slip dislocations releasing seismic/acoustic energy over a wide range of slip magnitudes (Pollard & Segall 1987; Segall 1989). There appears to be no lower limit to the stress or fluid pressure fluctuation that can stimulate seismic/acoustic activity (Ziv & Rubin 2000).

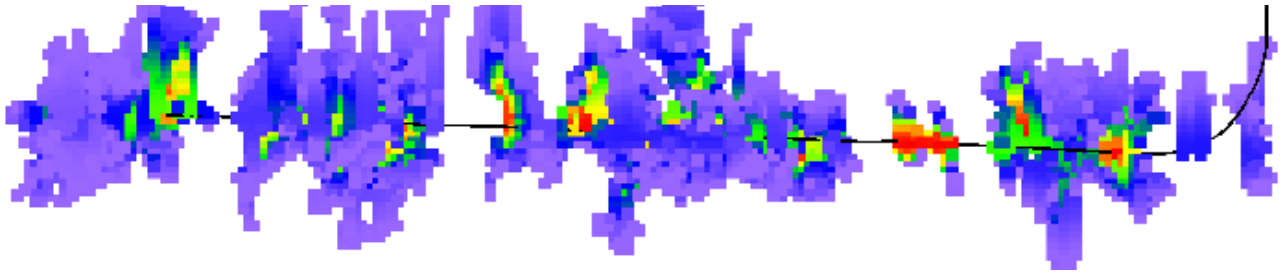

Fig 13. Second representation of Fig 12 shale reservoir wellbore seismic semblance sequence along wellbore. Colors denote spatial distribution of semblance magnitude; warm colors are high semblance, cool colors are low semblance.

The warmer colors in Fig 13 denote crustal zones along the wellbore that are particularly active in response to fluid injection during hydrofracturing. Such crustal zones are likely equivalent to feed zones observed in geothermal wells (e.g., Sewell et al 2013). Fig 14 illustrates the population distribution of semblance values in Fig 13. The top plot-pair of Fig 14 plots shows the spatial and statistical distributions of semblance magnitudes in the Fig 13 event sequence; the spatial distribution is clustered, and the semblance magnitude population is lognormally distributed. A hypothetical uncorrelated random spatial sequence of semblance events along the wellbore is shown the lower plot-pair; the random spatial sequence is non-clustered, and the magnitude distribution is normal. The contrast between the observed spatial correlations and associated lognormality of Fig 13 and the uncorrelated hypothetical case of Fig 14 is consistent with Fig 1-9 observation of *in situ* poroperm processes and structures.

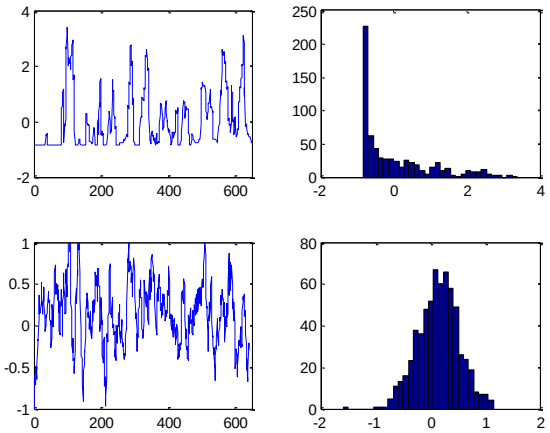

Fig 14. (Top) Plot and frequency distribution of Fig 13 semblance magnitude sequence normalized to zero-mean/unit variance format. (Bottom) Hypothetical sequence plot and distribution of absolute value of uncorrelated random sequence that is windowed to simulate finite spatial resolution, then normalized to zero-mean/unit variance format. Clustering in the Fig 13 semblance data sequence may reflect in part the finite spatial resolution of the data but likely also indicates the natural clustering tendency of fracture systems. Lognormality of the observed semblance magnitudes is inconsistent with the null hypothesis of uncorrelated randomness in the crustal fracture properties.

Fig 15 expands the scale of Fig 10-14 pressure-stimulated shale body seismic monitoring phenomenology to the spatial scale of geothermal field exploitation. Four map views 5km on a side show the systematic time evolution of seismic-noise response to wellbore pressure stimulation in a shale reservoir. In each map view, red lines denote regions identified by Fig 10-11 surface seismic array data processing as having high degrees of seismic event spatial semblance associated with spatially coherent porosity/permeability structures. Wellbore pressurisation at the center of the section initiates a slight smudge of reservoir seismic slip activity seen at the center of the upper-left section. In the succeeding sequence of snap-shots, the initial smudge grows in intensity and spatial scope as the induced fluid pressure field leaks into the formation and connects to crustal volume elements everywhere. In areas of sufficient poroperm spatial connectivity, the time-evolving induced pressure field destabilizes the high poroperm structures that are connected to the central wellbore poroperm structure (smudged areas) while not particularly affecting high poroperm structures that are not particularly connected to the central wellbore structure. Thus smudges thus partition the shale reservoir into more-connected flow systems and less-connected flow systems. One can readily translate such degree of spatial flow-structure mapping into a geothermal reservoir operation drilling plan to eliminate a great deal of uncertainty, guesswork, and inefficiency.

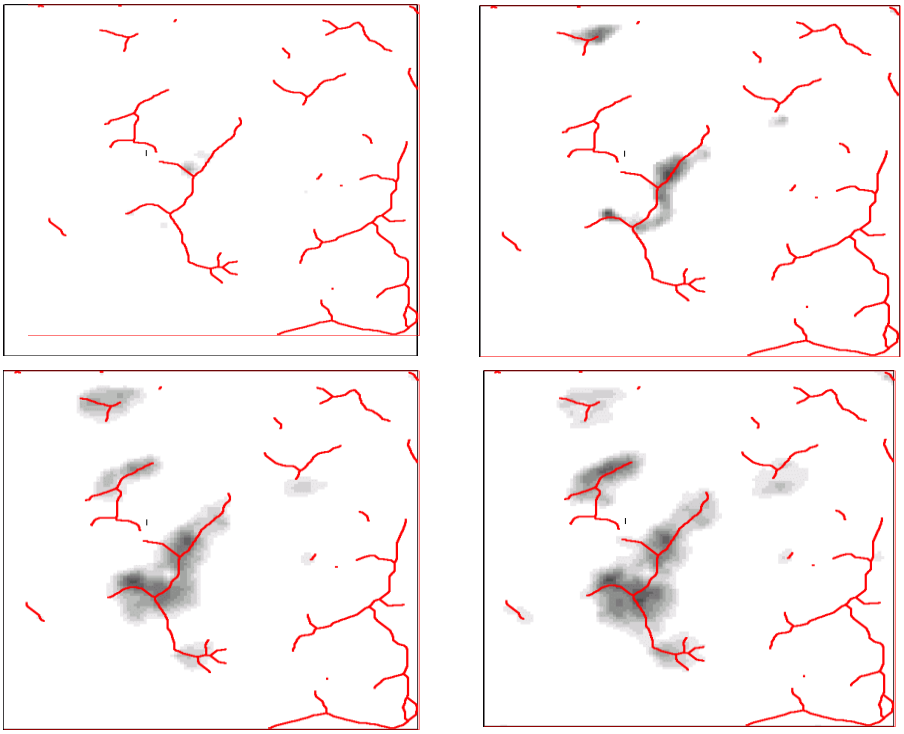

Fig 15. (Top-left to lower-right) Map views of spatiotemporal sequence of low-level geocritical seismic activity induced by hydraulic fracturing of horizontal wellbore in center of the map sections. Map sections are 5km on a side. Temporal sequence interval is 1 minute. Red lines indicate high seismic semblance structures previously inferred from background seismic monitoring by surface seismic array (see Figs 10-11). Sequence of black-tinted areas indicate time-evolving seismic activity beginning at wellbore and extending along the connected semblance structure but also jumping to neighbor semblance structures. Stimulated fluid pressure leaks into the crustal medium to destabilize regions of high porosity/permeability. Red lines thus represent targets for drilling into areas of high porosity/permeability and hence fluid flow.

5. SUMMARY/CONCLUSIONS

Fig 15 illustrates scope of surface array seismic monitoring that can be applied to geothermal fields. Geothermal fields are invested with convective fluid flow that generate locale seismic activity. Heretofore seismic observation of geothermal fields has focused on the microseismicity population of individually detectable events (e.g., Sewell et al 2013). In the course of microseismic monitoring of active reservoirs, however, it has become questionable if it is possible to locate individual events with sufficient accuracy to develop a clear model of major structural elements, in particular those structures relevant to important reservoir flow. In the case of geothermal fields, this emerging limitation of microseismic data can be traced in part to the complexity of the velocity structure of highly disrupted sequences of pyroclastic flows, and in part to the difficulty of acquiring information about the seismic-velocity structure of geothermal fields. Whatever the underlying causes, it has not transpired that microseismicity-structure information has proved itself capable to guiding geothermal field operators to refining their drill site selection strategy.

Neither of the velocity structure complications affecting geothermal fields applies in any great degree to currently producing shale reservoir plays. Shale reservoir plays are typically surveyed by standard surface seismic reflection methods yielding a detailed velocity model, which in turn is supplemented by a large number of perforation shots associated with hydrofracking stimulation along extended-reach horizontal wellbores. It is emerging, however, that shale reservoir well production/productivity is notably lognormal, and there has been little or no application of microseismic data to deciding where to drill or hydrofracture in shale reservoirs (IEA 2012). It can be supposed that the greater spatial detail afforded by the reservoir flow-structure imaging

demonstrated by Geiser et al (2006a-b, 2012) for surface-sensor array event detection and location will address the fundamental limitations of reliable flow-structure information endemic to microseismicity data.

The present discussion recasts seismic monitoring of geothermal fields in terms of low-level seismic event semblance images to take advantage of the high level of background noise that is fundamentally coupled to *in situ* fluid flow structures. This imaging process requires investment in acquiring velocity models of unprecedented accuracy for geothermal fields. There is no reason to believe, however, that the steady history of ever-increasing seismic array channel count leading to ever-increasing seismic imaging accuracy and fidelity in standard geological formations cannot be adapted to a geothermal setting by suitably adapting the multi-channel data processing capability of surface seismic imaging. Heretofore seismic imaging of geothermal fields has been limited to either low-event-count microseismic data or to surface sourcing. Low-level seismic event semblance imaging addresses both these prior imaging deficiencies. Low-level seismic event noise generation in geothermal areas is fundamentally coupled to the precise flow-structure observations that are sought. Sources of significance are naturally occurring at depth rather than assembled to operate at the surface. Refraction seismic sourcing into a dense surface sensor array can generate essentially arbitrarily accurate velocity models by which to process surface seismic array data. Seismic array listening time is an essentially low cost means to increased spatial resolution. For initial purposes, the subsurface spatial resolution problem is considerably relaxed from that associated with current shale reservoir practice. Identifying/locating *in situ* flow structures at a voxel resolution of 25m-50m would give a huge boost to drilling confidence at a tiny fraction of cost of a single well, let alone multiple wells. Subsequent detailed seismic semblance imaging of particular areas could likely refine the voxel resolution to more accurately guide drill siting to precisely the *in situ* flow-active targets demanded by geothermal power production.

Accompanying Papers I (Leary et al. 2015) & III (Pogacnik et al. 2015) have as their joint theme the strong limitation of thermal conductivity on EGS as a source of commercial heat energy. Central to the arguments of I & III is the importance of achieving advective flow in the larger context of ultimate conductive thermal recharge of crustal heat exchange volumes. This perspective is informed by noting, as in I, that virtually all commercial geothermal heat energy extraction occurs in connection with *in situ* convective (advective) flow systems. For EGS as primarily focused on conduction-limited crustal heat resource, this puts a premium on creating interior advective flow systems matched to exterior conductive recharge flow. But achieving this result for EGS crustal volumes confronts the same problems of complex, heterogeneous, spatially erratic *in situ* flow processes here addressed *re* better drill site targeting for better use of hydrothermal flow system resources. If, as seems probable, growth of geothermal energy acquisition and use in the immediate future lies in improved use of existing/proven resources, we can expect to use the reservoir imaging technology outlined here in the largest possible geothermal energy context:

- Reversing the steady decline of existing geothermal fields;
- Extending the spatial reach of known fields;
- Bringing on line more marginal fields.

Each of these goals has its own commercial worth, but together they have a larger role to play in understanding *in situ* flow as physical process far more complex than hitherto understood. Making steady concerted progress in understanding present geothermal resources can be the key to opening the future to expanded access to crustal heat.

REFERENCES

Ahrens LH (1963) Lognormal-type distributions in igneous rocks – IV, *Geochmica Cosmochim Acta* 27, 333-343.

Bennion DW & Griffiths JC (1966) A stochastic model for predicting variations in reservoir rock properties, *Soc. Petrol. Eng. Jour., Trans. ATME* 237, 9-16.

Crampin S (1994) The fracture criticality of crustal rocks, *Geophysical Journal International* 118, 428-438.

de Wijs HJ (1951) Statistics of ore distribution. Part I: frequency distribution of assay values, *J. R. Neth. Geol. Min. Soc. New Ser.* 13, 365–375.

de Wijs HJ (1953) Statistics of ore distribution Part II: theory of binomial distribution applied to sampling and engineering problems, *J. R. Neth. Geol. Min. Soc. New Ser*. 15, 125–124..

Dolan SS, Bean CJ & Riollet B (1998) The broadband fractal nature of heterogeneity in the upper crust from petrophysical logs, *Geophys. J. Int*. 132, 489-507.

Geiser, P., J. Vermilye, R. Scammell, S. Roecker, 2006a, Seismic Emission Tomography 1: Seismic used to directly map reservoir permeability fields: Oil & Gas Journal, v. 104, no. 46 6p.

Geiser, P., J. Vermilye, R. Scammell, S. Roecker, 2006b, Seismic Emission Tomography - 2: Seismic used to directly map reservoir permeability fields: Oil & Gas Journal, v. 104, no. 47, 6p.

Geiser P., A. Lacazette, and J. Vermilye, 2012, Beyond 'dots in a box': an empirical view of reservoir permeability with tomographic fracture imaging, *First Break* 30, p. 63-69.

Gerst MD (2008) Revisiting the Cumulative Grade-Tonnage Relationship for Major Copper Ore Types, *Economic Geology* 103, 615–628.

Grant MA (2009) Optimization of drilling acceptance criteria, *Geothermics* 38, 247–253.

Gupta HK (2002) A review of recent studies of triggered earthquakes by artificial water reservoirs with special emphasis on earthquakes in Koyna, India, *Earth-Science Reviews* 58, 279–310.

Hewett TA (1986) Fractal distributions of reservoir heterogeneity and their influence on fluid transport, SPE Paper 15386, *61st SPE Annual Technical Conference*, New Orleans.

IFC (2013) *Success of Geothermal Wells: A global study*, International Finance Corporation, Washington DC, 80pp.

International Energy Agency (2012) Special Report: Golden Rules for Golden Age of Gas, *International Energy Agency*, www.iea.org; http://www.iea.org/publications/ freepublications/publication/WEO2012_GoldenRulesReport.pdf, 150p.

Kaufman GM (1963) *Statistical Decision and Related Techniques in Oil and Gas Exploration*, Prentice-Hall, Englewood Cliffs, NJ.

Koch GS & Link RF (1971) The coefficient of variation; a guide to the sampling of ore deposits, *Economic Geology* 66, 293-301.

Law J (1944) A statistical approach to the interstitial heterogeneity of sand reservoirs, Technical Publication 1732, *Petroleum Technology* 7, May 1944.

Leary P, Malin P, Geiser P, Pogacnik J, Rugis J & Valles B (2015) Flow Lognormality & Spatial Correlation in Crustal Reservoirs – I: Physical Character & Consequences for Geothermal Energy, WGC2015, 19-24 April 2015, Melbourne AU.

Leary P, Malin P, Pogacnik J, Rugis J, Valles B & Geiser P (2014) Lognormality, $\delta\kappa \sim \kappa\, \delta\varphi$, EGS, and all that, *Proceedings 39th Stanford Geothermal Workshop*, February 24-26 2014, Stanford University, CA.

Leary PC, Malin PE, Ryan GA, Lorenzo C & Flores M (2013) Lognormally distributed K/Th/U concentrations – Evidence for geocritical fracture flow, Los Azufres geothermal field, MX, Proceedings Geothermal Resources Council 36th Annual Conference, 29 Sep – 3 Oct, Las Vegas NV.

Leary P, Pogacnik J & Malin P (2012) Fractures ~ Porosity --> Connectivity ~ Permeability --> EGS Flow Stimulation, *Proceedings 36th Geothermal Resources Council 36th Annual Conference*, 30 Sep – 3 Oct, Reno NV.

Leary PC (2002a) Fractures and physical heterogeneity in crustal rock, in *Heterogeneity of the Crust and Upper Mantle – Nature, Scaling and Seismic Properties*, J. A. Goff, & K. Holliger (eds.), Kluwer Academic/Plenum Publishers, New York, 155-186.

Leary PC (2002b) Numerical simulation of first-order backscattered P- and S-waves for time-lapse seismic imaging in heterogeneous reservoirs, *Geophysical Journal International* 148, 402-425.

Leary PC (1997) Rock as a critical-point system and the inherent implausibility of reliable earthquake prediction, *Geophysical Journal International* 131, 451-466.

Leary PC (1995) The cause of frequency-dependent seismic absorption in crustal rock, *Geophysical Journal International* 122, 143-151.

Leary PC (1991) Deep borehole log evidence for fractal distribution of fractures in crystalline rock. *Geophysical Journal International* 107, 615-628.

Leary PC & Al-Kindy F (2002) Power-law scaling of spatially correlated porosity and log(permeability) sequences from north-central North Sea Brae oilfield well core, *Geophysical Journal International* 148, 426-442.

Leary P & Abercrombie RE (1994a) Frequency dependent crustal scattering and absorption at 5-160 Hz from coda decay observed at 2.5 km depth, *Geophysical Research Letters* **21**, 971-974.

Leary P & Abercrombie RE (1994b) Fractal fracture scattering origin of S-wave coda: spectral evidence from recordings at 2.5 km, *Geophysical Research Letters* **21**, 1683-1686.

Mabee SB (1999) Factors influencing well productivity in glaciated metamorphic rocks, *Ground Water* 37, 88-97.

Maharjan M (2011) Interpretation of domestic water well production data as a tool for detection of transmissive bedrock fractured zones under cover of the glacial formations in Geauga County, Ohio, M.S. Thesis, Kent State University.

Malin P, Leary P, Shalev E, Rugis J, Valles B, Boese C, Andrews J & Geiser P (2015) Flow Lognormality and Spatial Correlation in Crustal Reservoirs: II – Where-to-Drill Guidance via Acoustic/Seismic Imaging, WGC2015, 19-24 April 2015, Melbourne AU.

Marsan D & Bean CJ (1999) Multiscaling nature of sonic velocities and lithology in the upper crystalline crust: Evidence from the KTB main borehole, *Geophysical Research Letters* 26, 275-278.

Petroleum Economist (2009) Unlocking the value of the world's geothermal resources, Euromoney Institutional Investor PLC, London, UK

Pogacnik J, Leary P, Malin P, Geiser P, Rugis R & Valles B (2015) Flow Lognormality and Spatial Correlation in Crustal Reservoirs: III -- Natural Permeability Enhancement via Biot Fluid-Rock Coupling At All Scales, WGC2015, 19-24 April 2015, Melbourne AU.

Pollard, D. D., and P. Segall, 1987, Theoretical displacements and stresses near fractures in rock with applications to faults, joints, veins, dikes, and solution surfaces, in B. K. Atkinson, ed., Fracture Mechanics of Rock, Academic, San Diego, CA., 1987.

Ricciardia K.L., G.F. Pinder& K. Belitz , 2005. Comparison of the lognormal and beta distribution functions to describe the uncertainty in permeability, *Journal of Hydrology* 313, 248-256.

Segall P., 1989, Earthquakes triggered by fluid extraction. Geology 17(10), 942–946.

Sewell SM, Cumming W, Bardsley CJ, Winick J, Quinao J, Wallis IC, Sherburn S, Bourguignon S & Bannister S (2013) Interpretation of microearthquakes at the Rotokawa geothermal field, 2008 to 2012, *Proceedings 35th New Zealand Geothermal Workshop*, Rotorua, NZ.

Simpson DW (1976) Seismicity changes associated with reservoir loading, *Engineering Geology* 10, 123-150.

Simpson DW & Negmatullaev SK (1980) Induced seismicity at Nurek Reservoir, Tadjikistan, USSR, *Bulletin of the Seismological Society of America* 70, 1561-1586

Simpson DW, Leith WS & Scholz CH (1988) Two types of reservoir-induced seismicity, *Bulletin of the Seismological Society of America* 78, 2025-2040.

Sanyal SK & Enedy SL (2011) Fifty years of power generation at the Geysers geothermal field, California – The lessons learned, *Proceedings* 36th Workshop on Geothermal Reservoir Engineering, Stanford University, January 31 - February 2.

Shiomi K, Sato H & Ohtake M (1997) Broadband power-law spectra of well-log data in Japan, *Geophys. J. Int.* 130, 57-64.

US Energy Information Administration (2011) *Distribution and Production of Oil and Gas Wells by State*, www.eia.gov/pub/oil_gas/petrosystem/all-years-states.xls.

Warren JE & Skiba FF (1964) Macroscopic dispersion, *Society of Petroleum Engineers Journal* SPE648, 215-230.

Zikovsky L & Chah B (1990) The lognormal distribution of radon concentration in ground water, *Ground Water* 28, No. 5, 673-676.

Ziv A & Rubin AM (2000) Static stress transfer and earthquake triggering: No lower threshold in sight?, *Journal of Geophysical Research* 105, 631-642.